Lecture 8: Pinning and depinning in one and two dimensions

Edgar Knobloch: notes by Rosalind Oglethorpe and Felicity Graham
with substantial editing by Edgar Knobloch

January 10, 2013

1   Pinning region (SH23)

Recall that the Swift-Hohenberg (SH) equation has multiple steady states in a 'snakes-and-ladders' structure, which is contained in a region of r called the snaking or pinning region. The width of this region can be understood on the basis of a geometrical picture of phase space behavior and a physical ("intuitive") picture in terms of front pinning. The pictures are complementary as well as useful.

1.1   Mathematical explanation of the pinning region

The time-independent SH equation is of fourth order in space,

$$u_{xxxx} + 2q_c^2 u_{xx} + (q_c^4 - r)u = f(u) \tag{1}$$

so the phase space is four-dimensional. This equation conserves the spatial Hamiltonian

$$H = -\frac{1}{2}\left(r - q_c^4\right)u^2 + q_c^2 u_x^2 - \frac{1}{2}u_{xx}^2 + u_x u_{xxx} - \int_0^u f(v)dv, \tag{2}$$

i.e., $dH/dx = 0$. Since the homogeneous state $u_{xxx} = u_{xx} = u_x = u = 0$ corresponds to $H = 0$ any homoclinc orbit connecting this state, hereafter O, to itself must lie in the level set $H = 0$, i.e., in a three-dimensional surface in four dimensions. As explained in lecture 6 to find such homoclinics it is advantageous to look for a heteroclinic cycle between O and a periodic orbit γ that also lies in $H = 0$. Near this cycle we expect to find orbits homoclinic to O that start from O and wind a finite number of times around γ before returning to O.

Because of translation invariance periodic orbits of Eq. (1) are not isolated – for each H there is a continuous family of such orbits. In the following we pick $H = 0$ and select one representative from this family, for example by assigning the origin $x = 0$ to the maximum value of u along the orbit. We call the resulting orbit γ. A point on this orbit with phase ϕ relative to $x = 0$, $\gamma(\phi)$, will be a fixed point of a "time-T" map, where T is the (spatial) period of the orbit, and we may pick ϕ to correspond to a point of symmetry on γ, for example $\phi = 0$ [15]. Note that T depends in general on H. By construction the "time-T" map is two-dimensional and has two fixed points, O and $\gamma(\phi)$. The result of repeated application of the "time-T" map can therefore be represented in a plane, as shown in fig. 1. The figure shows the two fixed points as solid black points; these lie on a green line representing solutions with
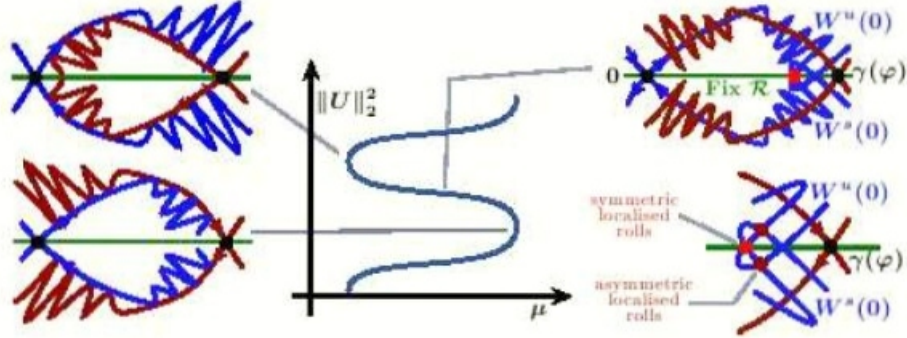
Figure 1: A cartoon of the stable and unstable manifolds for the fixed points O and $\gamma(\phi)$ in the planar representation, at different values of μ in the pinning region. From [15, 2].

the symmetry $u(-x) = u(x)$. The figure shows the intersections of the stable and unstable manifolds of O, labeled $W^{s,u}(O)$, with the surface $H = 0$. Both are one-dimensional and are shown in blue, and consist of points that approach O after an infinite number of backward and forward applications of the map. The intersection of corresponding (three-dimensional) center-stable and center-unstable manifolds of γ with $H = 0$ are shown in brown and are also one-dimensional. Since we are dealing with a discrete map these manifolds consist of discrete sequences of points obtained by applying the map to different points in the stable and unstable manifolds of these fixed points. Because of the discrete nature of the resulting two-dimensional dynamics we expect the unstable manifold $W^u(O)$ to intersect transversally with the center-stable manifold $W^s(\gamma)$ (top right panel in the figure). The point of intersection is simultaneously on both manifolds implying that forward iterations take it to $\gamma(\phi)$ while backward iterations take it to O, i.e., such a point is a heteroclinic point. Each image of this point, forward or backward, will also be a heteroclinic point since it must again lie on an intersection of these manifolds. Since the forward iterates accumulate on γ the unstable manifold $W^u(O)$ must execute increasingly wild gyrations near $\gamma(\phi)$ as indicated in the figure. This is a consequence of the Hamiltonian nature of Eq. (1) which implies that the "time-T" map is area-preserving. Thus the areas of the (primary) lobes are all the same and since the foot of the lobes shrinks towards $\gamma(\phi)$ their length must grow in proportion. Spatial reversibility implies that $W^s(O)$ undergoes identical behavior and hence that $W^u(O)$ and $W^s(O)$ must intersect. The primary intersections must lie on the green curve and hence correspond to solutions with $u(-x) = u(x)$ that lie simultaneously in $W^u(O)$ and $W^s(O)$ (large red dot). Such solutions represent symmetric homoclinic solutions of Eq. (1). Observe that since the primary intersections accumulate on $\gamma(\phi)$ there will in fact be an infinite number of such homoclinic solutions corresponding to symmetric localized structures of ever larger length. The figure also indicates that associated with each primary intersection there is a pair of secondary intersections (small red dots, bottom right panel in the figure). These do not lie in the green line and hence correspond to asymmetric homoclinic points, i.e., the rung states of lecture 7.

Figure 1 shows that the *heteroclinic tangle* described above is created, as the bifurcation
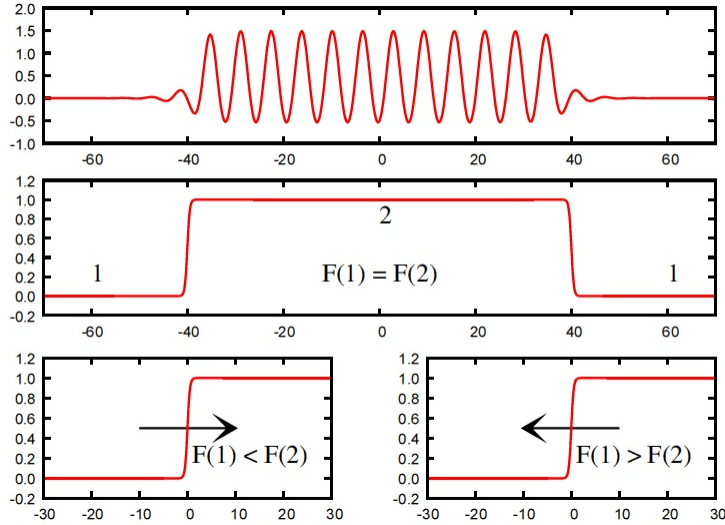
Figure 2: A cartoon of the motion of a front separating phase 1 (liquid) from phase 2 (gas) either side of the Maxwell point $F(1) = F(2)$ (bottom panels). The quantity F represents the free energy. The front is stationary only at the Maxwell point (middle panel). The top panel shows the case when phase 2 is a crystalline solid.

parameter μ (equivalently r) increases, at the point of first tangency between $W^u(O)$ and $W^s(\gamma)$ (top left panel) and destroyed at the point of last tangency (bottom left panel). Thus the snaking region is bounded on either side by the location of tangencies between these manifolds and no (long) localized states are present outside of the parameter interval between these two tangencies [2, 15].

An essentially identical picture applies to reversible but non-Hamiltonian systems since the fundamental properties of the heteroclinic tangle depend only on the presence of a transversal intersection between $W^u(O)$ and $W^s(\gamma)$ together with spatial reversibility. For this reason the geometrical picture sketched here has a far greater applicability than one may imagine at first sight. This is a consequence of the fact that a transversal intersection between manifolds cannot be destroyed by small perturbations in the parameter μ, i.e., it is a consequence of structural stability.

1.2 Physical explanation of the pinning region

Consider now the energetics of the system. The Lyapunov function F (defined in lecture 7) can be thought of as the free energy of the system. This allows us to compare the energy of the zero state and of the periodic state. Equilibria correspond to critical points of F, and without loss of generality we can define $F = 0$ at $u = 0$. We can calculate F for the periodic orbit with onset wavenumber q_c, which is a well-defined integral, and find the point where $F = 0$ for the periodic orbit. This construction define the "Maxwell point" $r = r_M$ by analogy with standard phase transitions, for example, a transition between a gas and a liquid (fig. 2). At a critical temperature T_c (equivalently r_c) the liquid (phase 1) and gas (phase 2) coexist with equal energy and the insertion of a front separating the
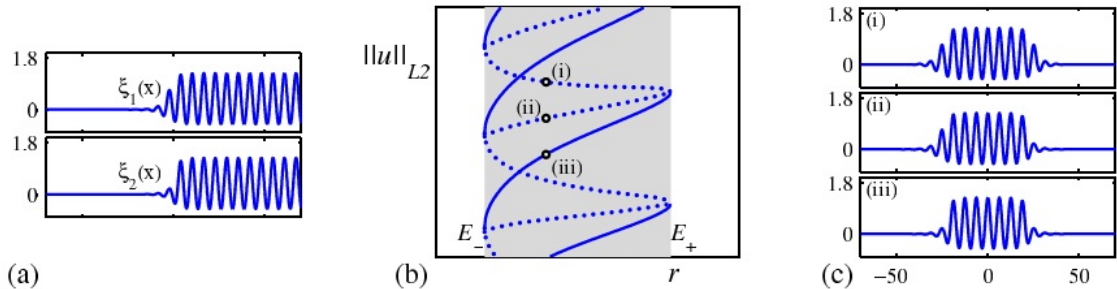
Figure 3: (a) The two types of fronts ξ_1 (unstable) and ξ_2 (stable) in SH23. (b) A section of the bifurcation diagram. (c) Three different localized states constructed from ξ_1 and ξ_2. From [3].

two states does not cost additional energy (middle panel in fig. 2). If the temperature is lowered (bottom left panel in fig. 2), $T < T_c$, the energy of the liquid phase is less than the energy of the gas phase, and we expect the gas to condense. In this case the front between the two phases moves into the gas phase, effectively replacing the gas with liquid. If the temperature is raised (bottom right panel in fig. 2), $T > T_c$ and the front will propagate to the left turning the liquid into gas. The front is therefore stationary only when $T = T_c$ (that is, the critical temperature can be thought of as the 'Maxwell temperature'). Now suppose that one of the phases is structured, for example a crystalline solid (top panel in fig. 2). Here, small temperature perturbations will not result in front motion as the front is held back by a "pinning potential" due to the structured state behind it [13]. This pinning allows stationary fronts over a range of T about T_c, and the temperature must be changed by a finite amount to overcome the effective pinning potential and allow the fronts to move. There are many coexisting steady states within the interval of temperatures around T_c, where the fronts are pinned since in this region it costs little to insert fronts between the two competing phases.

At each value of r in the pinning region one can identify two types of front, ξ_1 and ξ_2, as shown in fig. 3(a). These fronts can be placed back to back to contruct localized structures. The three different localized states that can be constructed from these fronts at each parameter value are shown in fig. 3(c), with the location of these states indicated in the bifurcation diagram in fig. 3(b) using solid dots. There are symmetric states with either (i) ξ_1 fronts at either end or (iii) ξ_2 fronts at either end; asymmetric states (ii) consist of one ξ_1 and one ξ_2 front. We can assign stability to these fronts and find that front (i) is unstable while front (ii) is stable. These stability assignments are indicated in fig. 3(b) by solid (stable) and dotted (unstable) lines. The pinning region can thus be thought of as an unfolding of the Maxwell point due to the heterogeneity of one of the states.

1.3 Wavelength selection (SH23)

Consider the wavenumber inside the localized structure. Computations show that the wavenumber (equivalently the wavelength) of the pattern depends on the value of r within the pinning region. This wavenumber is not given by minimizing the free energy F because
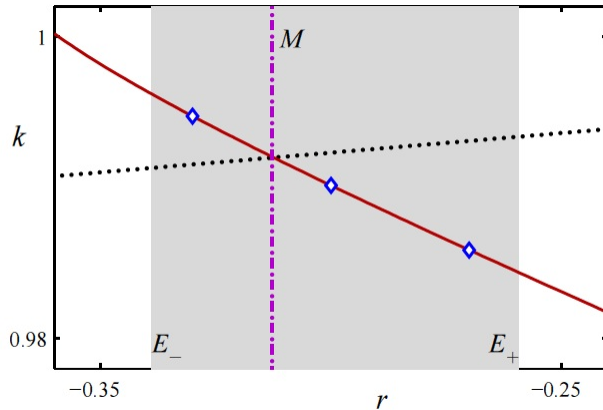
Figure 4: The wavenumber k found by minimizing F (dotted black line), minimizing F with the $H = 0$ constraint (solid red line) and results from numerical simulations (blue diamonds). The pinning region is shaded in grey. From [3].

of the $H = 0$ constraint required of all homoclinic orbits. Figure 4 shows that to the left of the Maxwell point $r = r_M$, k is higher than the Maxwell value, so the wavelength is less than the Maxwell wavelength. For $r < r_M$, the periodic state has a higher energy F than the zero state, so in the absence of pinning the fronts would move inwards eliminating the periodic state. However, in the pinning region they are prevented from moving by the pinning effect. Instead the energy difference between the two states manifests itself in a compression of the resulting steady structure. Conversely, for $r > r_M$ the periodic state has lower energy than the zero state, so in the absence of pinning the fronts would move outwards and the structure would grow. Since the fronts are prevented from moving by the pinning effect the structure instead stretches. The variation of $k(r)$ can be calculated by minimising F subject to the constraint $H = 0$, and the result agrees well with measurements from numerical calculations (fig. 4).

We remark that the presence of the fronts at either end leads to a unique wavenumber between them, however far apart the fronts are. This is in contrast to spatially *periodic* states for which there is an interval of stable wavenumbers within the so-called Eckhaus stability limits. Evidently wavenumber selection is very sensitive to what happens "at infinity" and in particular the boundary conditions applied there. We may say that the fronts collapse the Busse balloon [8].

1.4 The pinning region in parameter space

The extent of the pinning region for SH23 in the (r, b_2) plane is shown in fig. 5. The pinning region is shaded and bounded by two blue lines corresponding to first and last tangencies as explained above. The region is exponentially thin near its tip at $(0, \sqrt{27/38}q_c^2)$ [6]. Near the tip, i.e., when $r = \mathcal{O}(\epsilon^4)$ and $b_2 = \mathcal{O}(\epsilon^2)$, $\epsilon \ll 1$, the width of the snaking region is exponentially thin, of order $\epsilon^{-4} \exp(-\pi/\epsilon^2)$, a result that requires the use of exponential asymptotics [9].

Away from the exponentially thin region near $r = 0$, the snaking region broadens but

5
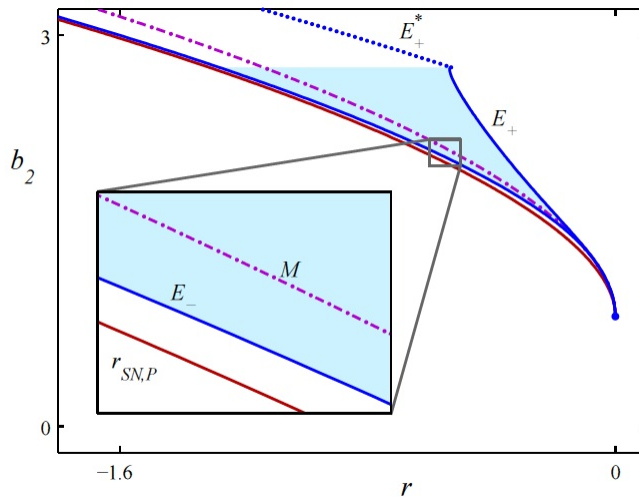
Figure 5: The pinning region (shaded in blue) for SH23 in the (r, b_2) parameter plane. The pinning region for SH35 is similar. From [3].

always straddles the Maxwell line, which is the purple dot-dash line in fig. 5. The red line shows the fold (saddle-node bifurcation) of the periodic orbit γ with wavenumber q_c. The snaking region tracks the fold, but does not reach it. A similar plot can be drawn for the SH35 equation [5].

Additional Maxwell points involving nontrivial homogeneous states are also present and considerably complicate the full picture [6]. These are responsible, for example, for the boundary E_+^* in fig. 5. In fact SH23 is still by no means completely understood.

2   Depinning

If r is moved sufficiently far from r_M the energy difference between the zero state and γ exceeds the pinning potential and the fronts *depin*. The resulting motion can be predicted by projecting SH23 onto the near-marginal eigenfunctions present at either edge of the pinning region.

At the boundary of this region the marginally stable amplitude eigenfunctions are localized near either front of the structure (see lecture 7). Near E_+, where the state of the system evolves towards the lower energy periodic state, this fact indicates incipient nucleation of new cells just outside the localized state. Direct integration of Eq. (1) reveals time-dependent growth of the structure via sequential nucleation of new cells (fig. 6(a)). The nucleation time depends on the distance from the edge of the pinning region, as indicated in fig. 6(b). The time diverges at the edge of the pinning region (where it takes an infinite amount of time to nucleate a new cell) and decreases as the distance from the pinning region increases. The speed of the front, which is a 'pushed front' because it propagates into a stable state [14], can be calculated from the time it takes to nucleate cells at the front. To the left of the pinning region (where the solution moves towards the lower energy zero state) the fronts move inwards via sequential annihilation of cells with the same dependence on
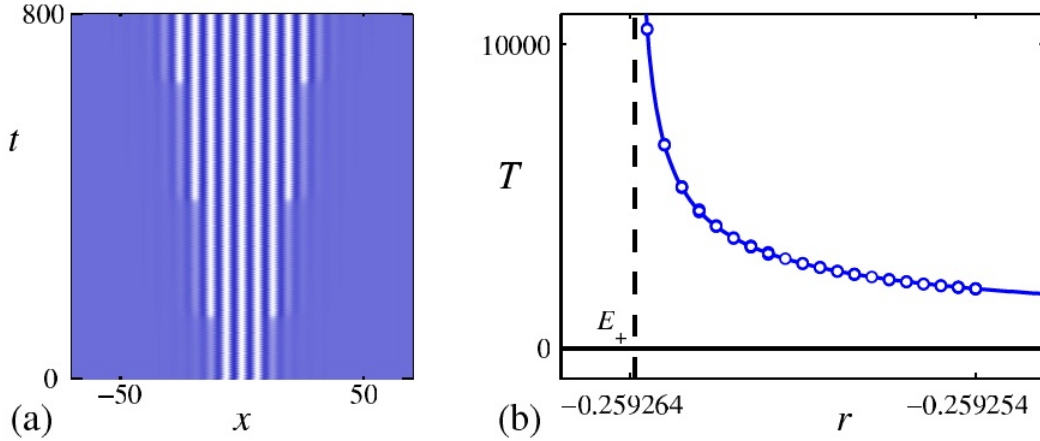
Figure 6: (a) Space-time plot of the evolution of a localized structure in time, and (b) the nucleation time T as a function of r. From [3].

the distance from E_- as in the E_+ case.

2.1 Theory

To calculate the speed of the front we need the time taken to nucleate (or annihilate) a cell [6]. For this purpose we suppose that

$$r = r(E_-) + \delta, \tag{3}$$

where $r(E_-)$ denotes the left edge of the pinning region and $|\delta| \ll 1$. Thus δ determines the distance away from the edge of the pinning region: if $\delta > 0$, then r is inside the pinning region and if $\delta < 0$ then r is outside the pinning region. We anticipate that nucleation takes place on an $\mathcal{O}(|\delta|^{-1/2})$ time scale and therefore introduce the slow time $\tau = |\delta|^{-1/2}t$. Finally we write

$$u(x,t) = u_0(x) + |\delta|^{1/2}u_1(x,\tau) + |\delta|u_2(x,\tau) + \mathcal{O}(|\delta|^{3/2}), \tag{4}$$

where $u_0(x)$ is one of the stationary localized states at the edge of the pinning region, assumed to be of even parity.

Substituting this Ansatz into SH23, we find at $\mathcal{O}(|\delta|^{1/2})$

$$\mathcal{L}[\mathrm{d}_x, u_0]u_1(x,\tau) = 0, \tag{5}$$

where $\mathcal{L}$ is the linearised SH operator evaluated at $r = r(E_-)$. The solutions of this problem[1] were found in lecture 7:

$$u_1(x,t) = a(t)\tilde{U}_{amp} + b(t)\tilde{U}_{ph} + c(t)\tilde{U}_G. \tag{6}$$

Of these marginal modes the amplitude mode $\tilde{U}_{amp}$ is even while the remaining two are odd. We may therefore suppose that the 'centre of mass' remains fixed and take $b = c = 0$.

---

[1]In the following we treat the exponentially small phase eigenvalue as zero.

Thus it suffices to determine the evolution of $a(t)$, the amplitude of the mode responsible for depinning.

For this purpose we proceed to $\mathcal{O}(|\delta|)$ obtaining

$$\mathcal{L}[\mathrm{d}_x, u_0]u_2(x, \tau) = \partial_\tau u_1 - [\mathrm{sgn}(\delta)u_0 + b_2 u_1^2 - 3u_0 u_1^2]. \tag{7}$$

For the ordering assumed in the Ansatz (4) to remain valid on the timescale $\tau = \mathcal{O}(1)$ the solution $u_2(x, \tau)$ must remain $\mathcal{O}(1)$ on this timescale. This will only be so if an appropriate solvability condition is imposed on the right hand side of Eq. (7). To find this solvability condition we apply the so-called Fredholm alternative [] and multiply Eq. (7) by $\tilde{U}_{amp}$ and integrate over x from $-\infty$ to ∞. Since $\mathcal{L}[\mathrm{d}_x, u_0]$ is self-adjoint the left hand side vanishes after integration by parts, leaving the condition

$$\alpha_1 \mathrm{d}_t a = \alpha_2 \mathrm{sgn}(\delta) + \alpha_3 a^2, \tag{8}$$

where

$$\alpha_1 \equiv \int_{-\infty}^{\infty} \tilde{U}_{amp}^2 \mathrm{d}x, \quad \alpha_2 \equiv \int_{-\infty}^{\infty} u_0 \tilde{U}_{amp} \mathrm{d}x, \quad \alpha_3 \equiv \int_{-\infty}^{\infty} (b_2 - 3u_0) \tilde{U}_{amp}^3 \mathrm{d}x. \tag{9}$$

This is the required evolution equation for the amplitude of the nucleation mode. The nucleation time, which is the time T for the solution to move from one fold of the snaking branch to the next one below, is approximately the time taken for $a(\tau)$ to go from $-\infty$ to ∞. Writing this condition in terms of the original time we obtain

$$T_- = \frac{\pi \alpha_1}{(\alpha_2 \alpha_3 \delta)^{1/2}} \approx 4.388|\delta|^{-1/2}, \quad \delta < 0. \tag{10}$$

This prediction compares well with the simulation result

$$T_- \approx (4.57 \pm 0.34)|\delta|^{-0.499 \pm 0.006}, \quad \delta < 0. \tag{11}$$

The method can be similarly applied near the right edge of the snaking region, $r = r(E_+) + \delta$, $0 < \delta \ll 1$, with corresponding prediction

$$T_+ = \frac{\pi \alpha_1}{(\alpha_2 \alpha_3 \delta)^{1/2}} \approx 5.944\delta^{-1/2}, \quad \delta > 0, \tag{12}$$

and simulation result

$$T_+ \approx (6.04 \pm 0.18)\delta^{-0.501 \pm 0.003}, \quad \delta > 0. \tag{13}$$

The nucleation time, T, thus depends on the inverse square root of the distance from the folds in the snaking region. These are very well aligned high up the bifurcation diagram, so here T is independent of which fold is considered and the nucleation front therefore moves with constant speed. This is not so low down the snaking diagram where the folds do not line up with the edge of the pinning region.
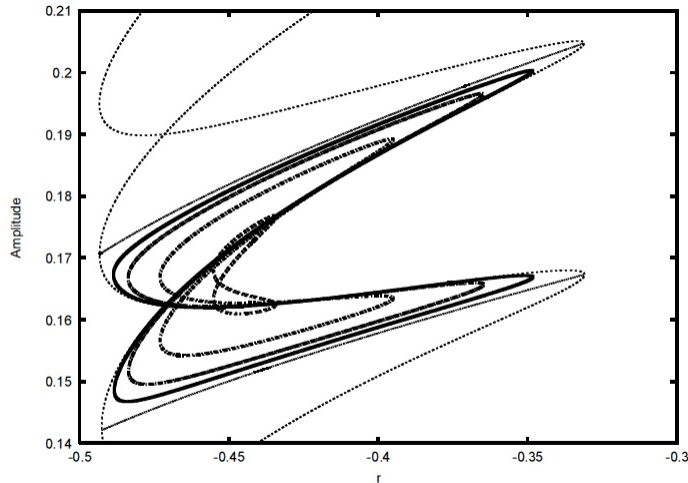
Figure 7: One set of isolas with $b_2 = 2$ and $\gamma = 0.05, 0.10, 0.20, 0.35$. From [4].

3 Broken symmetry and drift

It is interesting to examine the effect of broken spatial reversibility on the nucleation process. For this purpose we may add a dispersive term to SH23 to obtain

$$\partial_t u = \left(r - (1 + \partial_x^2)^2\right) u + \gamma \partial_x^3 u + b_2 u^2 - u^3. \tag{14}$$

We anticipate that when $\gamma \neq 0$ the solutions will drift, and therefore look for steady solutions drifting with speed c. Such solutions satisfy the ODE

$$0 = \left(r - (1 + \mathrm{d}_x^2)^2\right) u + c\mathrm{d}_x u + \gamma \mathrm{d}_x^3 u + b_2 u^2 - u^3, \tag{15}$$

where x is now the comoving coordinate and c is a nonlinear eigenvalue, i.e., c is determined as part of the solution.

Figure 7 shows the solution to this problem. One finds that the presence of dispersion destroys the snakes-and-ladders structure of the snaking region and that the drifting localized states fall on a stack of figure-eight isolas, one of which is shown in the figure. All the localized states now travel: $c = c(r)$ along each isola (not shown). Note in particular that as γ increases the isolas shrink and eventually disappear. Thus drifting localized structures are absent for large dispersion.

To the immediate right of the pinning region, $r = r(E_+) + \delta$ for $\delta \ll 1$, the nonzero value of γ leads to asymmetry between the nucleation rates associated with the leading and trailing fronts. This is shown in fig. 8, where all the patterns drift slowly to the right. For small enough δ, nucleation only occurs at the leading front but fails at the trailing front (fig. 8(a)). Further from the saddle-node, the rate of nucleation increases (as in the symmetric case) so that nucleation now takes place at both fronts, albeit at different rates. As a result the trailing front overcomes the slow drift of the structure downstream, and propagates upstream (fig. 8(b)). However, increasing γ can prevent nucleation at the trailing front so that the pattern only grows at the leading front (fig. 8(c)). The front speed for the asymmetric problem (15) can be calculated in much the same way as in the symmetric problem (see section 2.1) as discussed next.

9
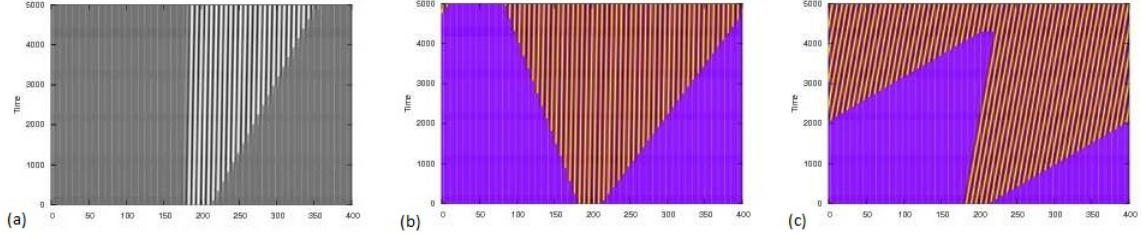
Figure 8: Space-time plots showing asymmetric front propagation when $b_2 = 2$: (a) $\gamma = 0.001, \delta = 0.00015$; (b) $\gamma = 0.001, \delta = 0.00065$; (c) $\gamma = 0.01, \delta = 0.00065$. From [4].

3.1 Theory

For small dispersion the drift speed c is expected to be of order γ. We therefore write $r = r(E_+) + \delta$, take $\gamma = \sigma|\delta|$, $\sigma = \mathcal{O}(1)$, and write []

$$u(x,t) = u_0(x + \theta(T)) + |\delta|^{1/2}u_1(x + \theta(T), \tau) + |\delta|u_2(x + \theta(T), \tau) + \ldots, \qquad (16)$$

where $\tau = |\delta|^{1/2}t$, $T = |\delta|t$ and $\theta(T)$ captures the drift of the leading order localized structure, i.e., $c = \theta_t = |\delta|\theta_T$. Note that the drift and nucleation occur on disparate timescales: the perturbations u_1 and u_2 drift on the same slow time T as u_0, but can also grow on a different, and faster, timescale τ. The leading order, $\mathcal{O}(1)$, terms are

$$r(E_+)u_0 - (1 + \partial_x^2)^2 u_0 + b_2 u_0^2 - u_0^3 = 0. \qquad (17)$$

This is the equation for steady solutions of the reversible SH23 equation with solutions $u_0 = u_0(x + \theta(T))$. At next order, $\mathcal{O}(|\delta|^{1/2})$,

$$\mathcal{L}[\partial, \sqcap_\prime]u_1 \equiv \left(r(E_+) - (1 + \partial_x^2)^2 + 2b_2 u_0 - 3u_0^2\right) u_1 = 0, \qquad (18)$$

and u_1, as in section 2.1, is a superposition of three (almost) marginal modes. Since the translation has been included by introducing the phase $\theta(T)$, the $\tilde{U}_G$ mode is already included. Thus

$$u_1 = a(\tau)\tilde{U}_{amp}(x + \theta(T)) + b(\tau)\tilde{U}_{ph}(x + \theta(T)). \qquad (19)$$

At $\mathcal{O}(|\delta|)$,

$$u_0'\theta_T + u_{1\tau} = \mathcal{L}u_2 + \text{sgn}(\delta)\, u_0 + \sigma u_0''' + (b_2 - 3u_0)u_1^2. \qquad (20)$$

Since the kernel of $\mathcal{L}$ is spanned by three independent solutions, the three marginal modes, we must impose three different solvability conditions on u_2. These will in turn determine the evolution of $\theta(T)$, $a(\tau)$ and $b(\tau)$.

To obtain the solvability conditions we multiply Eq. (20) in turn by the three marginal modes, u_0' (i.e., the Goldstone mode), $\tilde{U}_{amp}$ and $\tilde{U}_{ph}$, and integrate over x from $-\infty$ to ∞. The first solvability condition predicts the drift speed

$$\theta_t = -0.9663\gamma, \qquad (21)$$

which agrees well with the drift speed measured from numerical simulations. The solvability conditions for the phase and amplitude modes give coupled equations for a and b. However,

10

if the structure described by u_0 is long enough, the two fronts at either end decouple from one another (lecture 6) and the two equations reduce to [4]

$$(a \pm b)_\tau = \alpha_1 \mathrm{sgn}\delta \mp \beta\sigma + \alpha_3(a \pm b)^2. \tag{22}$$

We define the nucleation time at the leading front as

$$T_{leading} = \int_{-\infty}^{\infty} \frac{d\tau}{a-b} = \frac{\pi}{\alpha_3^{1/2}} \frac{1}{(\alpha_1\delta + \beta\gamma)^{1/2}} \tag{23}$$

and at the trailing front as

$$T_{trailing} = \int_{-\infty}^{\infty} \frac{d\tau}{a+b} = \frac{\pi}{\alpha_3^{1/2}} \frac{1}{(\alpha_1\delta - \beta\gamma)^{1/2}}. \tag{24}$$

The value of δ for which the nucleation time diverges corresponds to the value at which nucleation ceases, and is given by

$$\delta_c^{leading} = -\beta\gamma/\alpha_1 = -0.3543\gamma, \quad \delta_c^{trailing} = \beta\gamma/\alpha_1 = 0.3543\gamma. \tag{25}$$

These predictions agree well with numerical simulations [4].

4   Two-dimensional structures

We now consider the two-dimensional (2D) Swift-Hohenberg equations SH23

$$u_t = ru - (\nabla^2 + 1)^2 u + b_2 u^2 - u^3, \quad (x, y) \in \mathbb{R}^2, \tag{26}$$

and SH35

$$u_t = ru - (\nabla^2 + 1)^2 u + b_3 u^3 - u^5, \quad (x, y) \in \mathbb{R}^2. \tag{27}$$

In both these equations $u = u(x, y, t)$ and $\nabla^2 \equiv \partial_x^2 + \partial_y^2$. These equations are reversible in both x and y but steady state solutions still correspond to critical points of the Lyapunov energy function F. In 2D, there is a larger range of different types of localized structures that arise, including stripes, spots, targets, squares and hexagons. For a more extensive treatment of this topic, we refer the reader to [5].

4.1   Wall and body modes

Stripe-like localized structures in 2D (e.g. fig. 9) are only stable inside a subregion of the 1D pinning region (fig. 10). This is a consequence of the presence of distinct 2D instabilities that destabilize localized stripes that are stable in 1D. These instabilities can be divided into "wall" modes which are characterized by a y-dependent eigenfunction that is localized at the fronts, and "body" modes whose eigenfunction extends across the whole localized structure.

Figures 11(a,b) show the evolution of a wall mode in SH23. Depending on the parameters the excitation of the wall mode may lead to depinning (fig. 11(a)) with both inward and
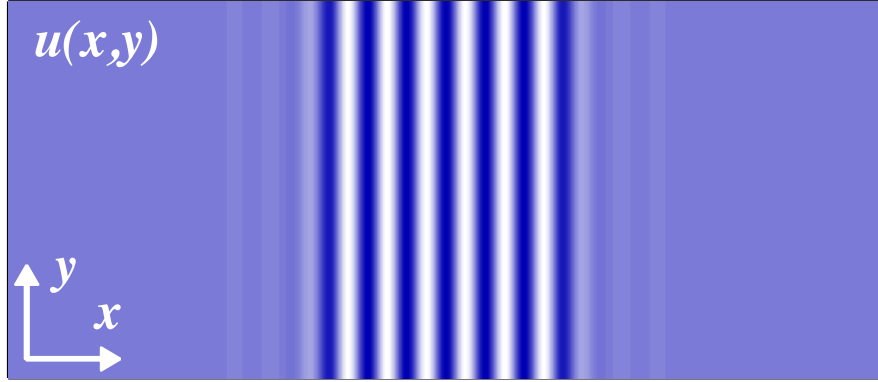
Figure 9: Localized 2D stripe in SH23. From [5].
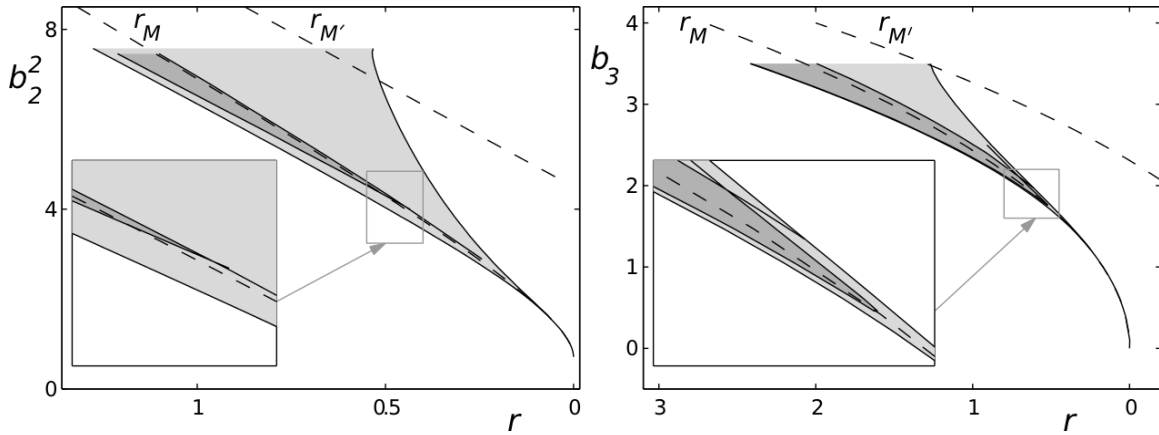
Figure 10: Stability regions for the 1D (light) and 2D (dark) localized structures in (a) SH23 and (b) SH35. From [5].

outward front propagation that converts the stripe state into a hexagonal array of spots that invades the whole domain. It is also possible to choose parameters such that there is not enough energy to depin the front connecting the structure to the background state (fig. 11(b)). In this case the outer fronts remain pinned and the instability propagates only inwards, turning the localized stripes into a localized patch of hexagons.

An example of the body mode is illustrated in fig. 11(c). As the mode evolves the whole structure buckles into a zigzag structure. In the case shown the buckling is strong enough to depin the fronts on either side resulting in the growth of a set of transverse stripes. The wavelength of the stripes is determined dynamically by the motion of the fronts and so is
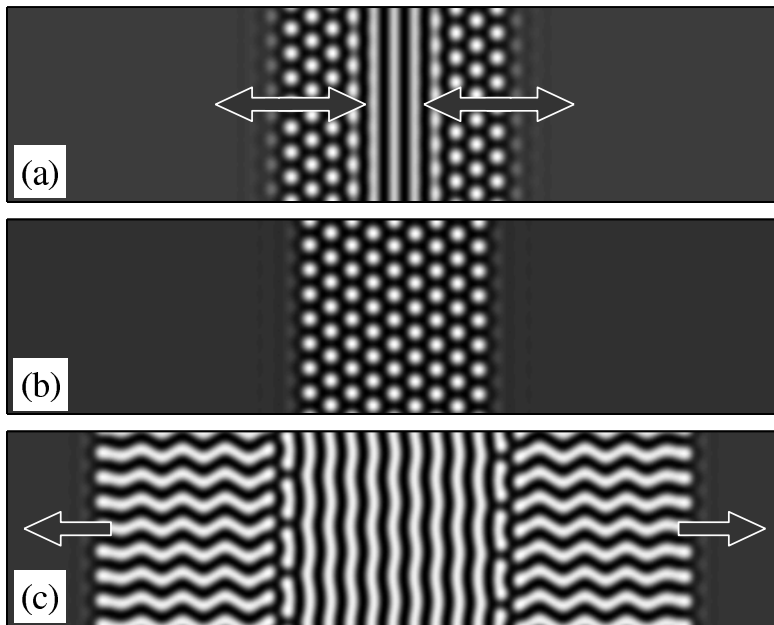
Figure 11: Evolution of (a,b) the wall mode, and (c) the body mode in SH23. From [5].

not the equilibrium wavelength. As a result the perpendicular stripes undergo their own zigzag instability that brings their wavelength closer to their equilibrium wavelength. SH35 undergoes similar instabilities but hexagonal coordination is no longer the preferred case. Instead the instabilities may generate moving fronts that undergo dendrite-like instabilities or lead to a dynamically selected labyrinthine pattern.

4.2 Two-dimensional spatially localized states

In the preceding section we have seen that time evolution can lead to stable localized states with nontrivial 2D structure. It is possible to follow solutions of this type numerically as a function of the parameters. Figure 12(a) from [1] shows one such steady-state solution of SH35 (right panel, corresponding to the red dot in the bifurcation diagram in the left panel). Following the solution numerically towards lower values of r (fig. 12(b)), we find that the amplitude $||u||_2^2$ begins to grow as the structure sends out "fingers" that extend farther and farther outwards. Since the front that connects this "finger" state with the background states only sees behind it a translation-invariant state no pinning takes place. In this case the pinning region is absent (we speak of *collapsed snaking*) and a heteroclinic cycle between the background state and the "finger" state is only present at a single parameter value. However, as we follow the solution in the other direction, we observe the formation of a rug-like structure associated with a snaking bifurcation diagram (fig. 12(c)). Here, the snaking is caused by the pinning of each front to stripes parallel to the front. It is remarkable that solutions of the form shown in figs. 12(b,c) in fact lie on the *same* solution branch.
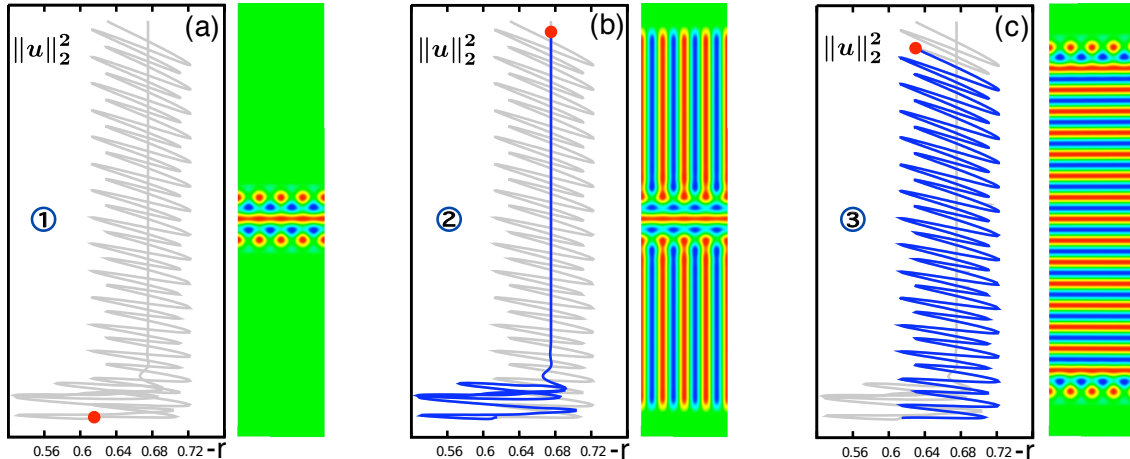
Figure 12: Bifurcation diagram of a localized stripe pattern in SH35. (a) A localized state identified through time integration. (b) Collapsed snaking. (c) Snaking. Each figure shows the appropriate portion of the bifurcation diagram (left panel) and the solution profile $u(x, y)$ (right panel) corresponding to the location indicated by the red dot. The profiles are shown with x vertically and y horizontally. From [1].

It is useful to think of structures such as that shown in fig. 12(b) in terms of a phase space representation, treating x as an unbounded time-like variable while y remains bounded (with Neumann boundary conditions imposed). This description is analogous to that employed in fig. 1: in fig. 13(a) the black dot represents the zero state while the red point represents an extended state of periodic stripes with finite y-wavenumber that fills the whole domain. A connection (1) between these two fixed points in the phase plane represents a front connecting the zero state to the pattern state (a heteroclinic orbit). An excursion (2) from the patterned state back to itself represents a defect in the patterned state. Spatial reversibility implies the existence of a complete heteroclinic cycle. As in 1D, numerical calculations identify homoclinic orbits with exactly this template, such as state (3) in fig. 13(b).

Figure 14 shows a detail of the bifurcation diagram for SH35. The sequence of transitions along the snaking branch produces alternating stable and unstable states, which grow in space. The growth mechanism is slightly different at points 3 and 7 compared with points 1, 5 and 9 owing to the Neumann boundary conditions in y used in the calculation. This leads to the observed misalignment of successive folds.

The rug-like structures in fig. 14 are just one set of localized structures present in this system; however, other structures are present as well. For example, it is possible to produce odd rug-like structures that also snake (dotted grey line in fig. 15). There are also rungs (blue line of fig. 15) of asymmetrical states that connect even states (solid grey line in fig. 15) to odd states. These Z-shaped rungs are unstable throughout as indicated by the eigenvalues shown in fig. 15(a). However, S-shaped rungs connecting even states to even states possess a stable middle segment (fig. 16).

Other structures that arise in 2D are checkerboard rugs (this live on isolas, of which
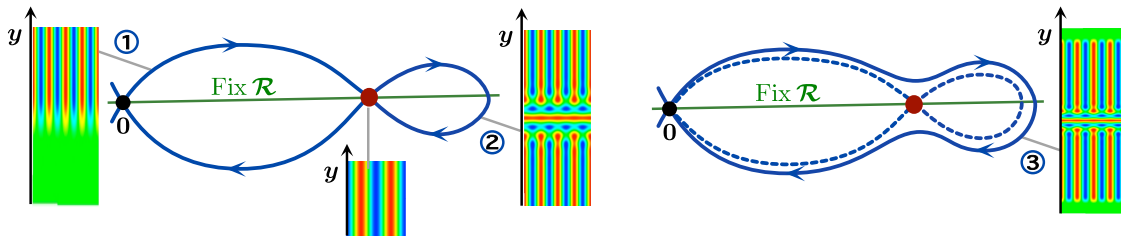
Figure 13: Phase plane description of collapsed snaking. From [1].
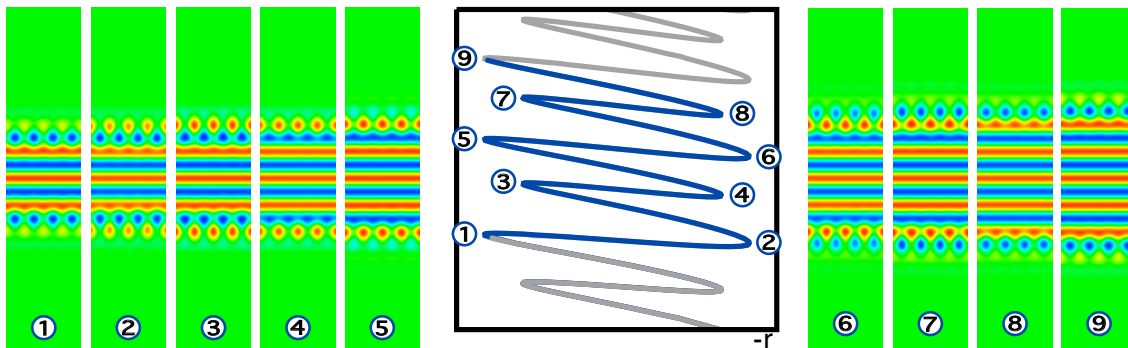
Figure 14: A section of the snaking branch from fig. 12 and the corresponding solution profiles at successive folds. From [1].

there is likely an infinite stack; fig. 17) and barrel-shaped structures (fig. 18). The latter are of particular interest since the fronts on the left and right are clearly pinned to the stripe pattern inbetween, while the curved boundaries likely experience weaker pinning arising from the circumferential wavelength gradient introduced by the curvature of the boundary. Perhaps of greatest interest are the leaf-like structures shown in fig. 19. These structures have a convex boundary that becomes, in some cases, concave near the cusps of the leaf. This fact implies that it is not possible to think of these structure as being produced by an effective surface tension since surface tension cannot produce structures that are concave. An understanding of the sharp, internally-generated cusp-like features of these structures represents a major challenge from the point of view of pde theory.

In SH23 the presence of the quadratic nonlinear term leads to a preference for hexagonal structures instead of stripes [8]. The different localized structures present in SH23 are discussed in [10]. As shown in fig. 20, localized hexagons, targets and spots occur in the different regions in the parameter plane as shown in fig. 20(a). The green line shows the fold of the extended periodic hexagonal pattern. Figure 20(b) shows the region near $r = 0$ and fig. 20(c) shows the bifurcation diagram for two different localized states, namely localized targets and hexagons. Pinning takes place as in 1D, although as the structure grows its effect decreases and snaking may collapse. We mention that target patterns behave quite
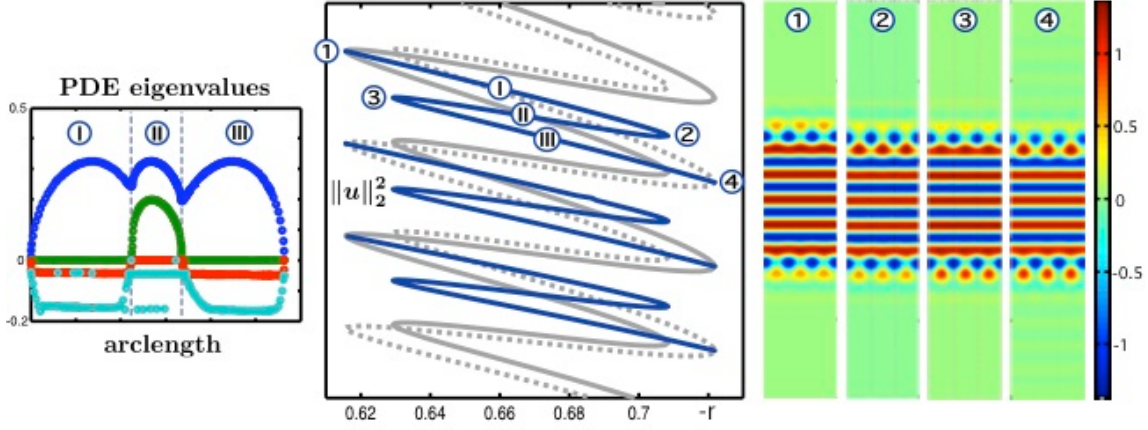
Figure 15: Unstable rung-like Z-shaped branches of asymmetrical states connecting even and odd parity branches (middle panel). The eigenvalues of the solutions as a function of arclength are shown in the left panel. The changes in the solution structure across the Z-shaped branch are shown in the right panel. From [1].
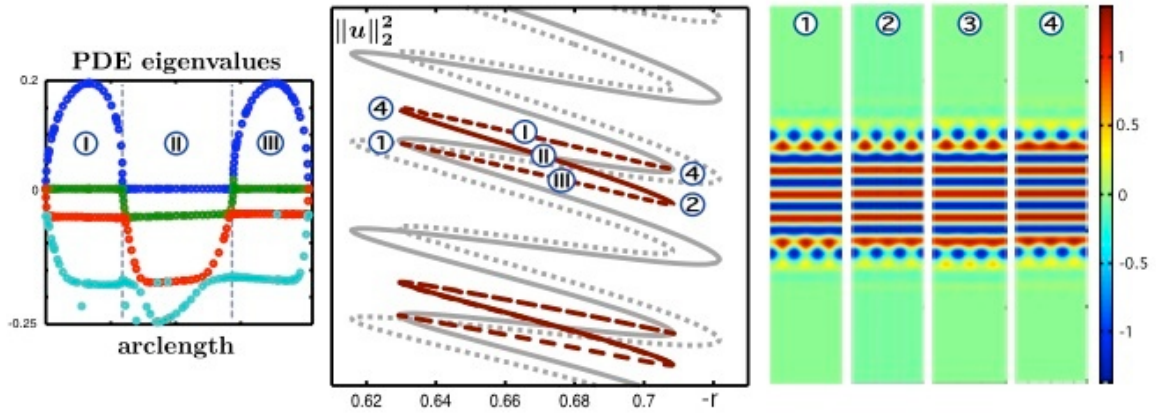
Figure 16: Rung-like S-shaped branches of asymmetrical states connecting even states to even states (middle panel). The eigenvalues of the solutions as a function of arclength (left panel) show that the middle segment is stable. The changes in the solution structure across the S-shaped branch are shown in the right panel. From [1].

differently from spots. The former are present only in the subcritical regime while spots are present even in the supercritical regime [11].[2] This important point may explain the

_____

[2]There are in fact two types of spots, spot A which is present regardless of the direction of branching of
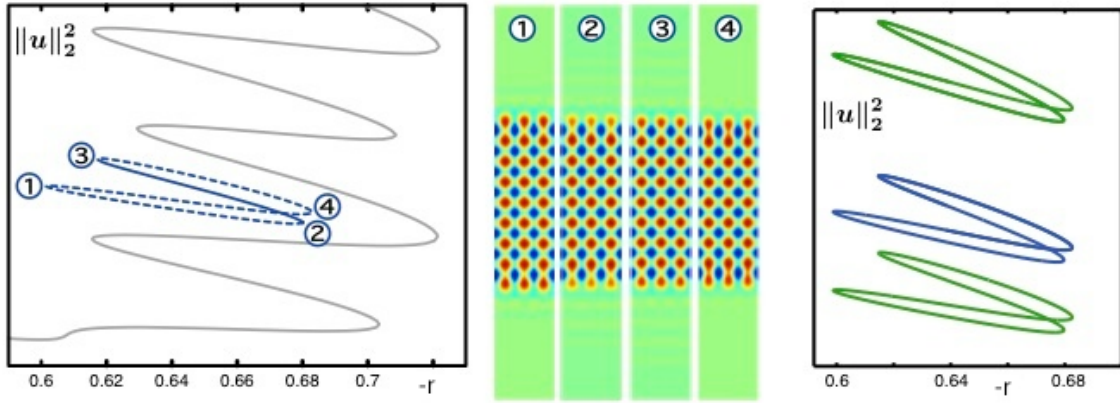
Figure 17: Left panels: localized checkerboard patterns on an isola. Solid line represents stable solutions. Right panel: part of a stack of such isolas with broader structures at the top and narrower structures at the bottom. From [1].
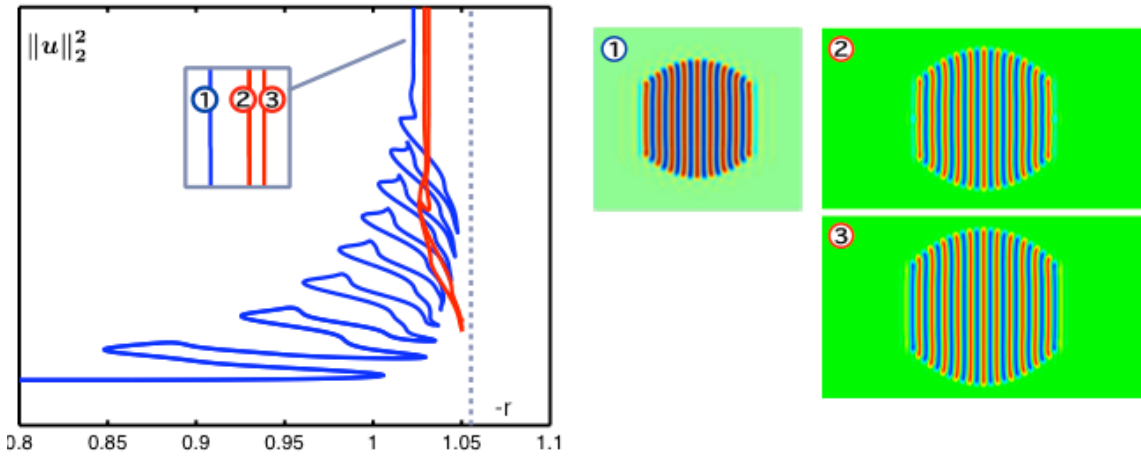
Figure 18: Left panel: barrel-shaped localized structures initially snake but large structures of this type lead to collapsed snaking. Right panel: subsidiary barrel-shaped structures differing by one stripe. From [1].

prevalence of spots in experiments.

Consider the hexagonal patch corresponding to the first fold in parameter space shown in fig. 21. It is possible to follow the solution branch numerically in parameter space [10]. At point 1, a regular hexagonal crystalline solution is present (note the "echoes" along the periphery the structure, which is a consequence of the oscillatory front between the

the stripe pattern and spot B which is only found in the subcritical regime [12].
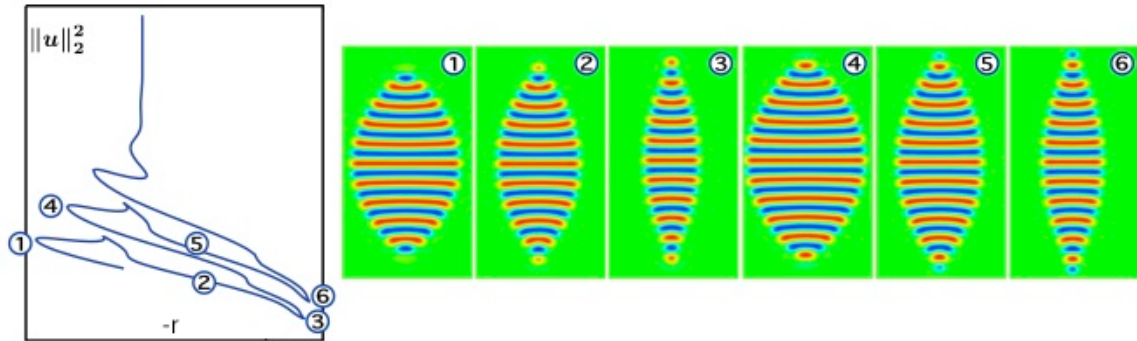
Figure 19: Planar leaf-like solutions of SH35. From [1].

hexagonal structure and the background state). By point 2 the structure has evolved by adding a cell at the mid-point of every edge. Further cells have been added symmetrically along the boundary by point 3, but the resulting structure is not hexagonal. The hexagonal structure reforms near point 4. Since the edges now consist of five cells apiece and the subsequent evolution differs from that just described. One must therefore proceed further up the solution branch on order to form a hexagonal structure with an even number of cells along each edge before the type of growth described in going from point 1 to point 4 recurrs. The misalignment of the folds provides an indication of the energy associated with the nucleation of cells in different locations along the edges. Comparison of the energy F for the different states shown in fig. 21 could provide an explanation why the hexagonal structure grows in the manner it does.

5   Oscillons

In lecture 6, we saw the difference between "standard" and "reciprocal" oscillons. Here, we consider steady, localized solutions to the forced complex Ginzburg-Landau (FCGL) equation. Our motivation for looking at this problem is two-fold. Firstly, oscillons have been observed in experiments. Secondly, the FCGL equation is similar to the SH equation when written in terms of the real and imaginary parts as coupled second order equations are equivalent to a problem of fourth order in space. However, the equation does not have a Lyapunov function, so we expect interesting dynamics.

5.1   Forced Ginzburg-Landau equation

Oscillons are typically subharmonic instabilities, and are easily observable in the vicinity of a subharmonic resonance (or 2:1 resonance) when an oscillatory system with natural frequency ω is driven with a driving frequency $\Omega \approx 2\omega$. If the detuning $\nu \equiv \omega - \Omega/2$ is small the system will oscillate with frequency $\Omega/2$ instead of ω. This oscillation is called a phase-locked oscillation since the phase of the driving and response remain in phase. Outside of this region, the response frequency is no longer locked to the forcing frequency and the
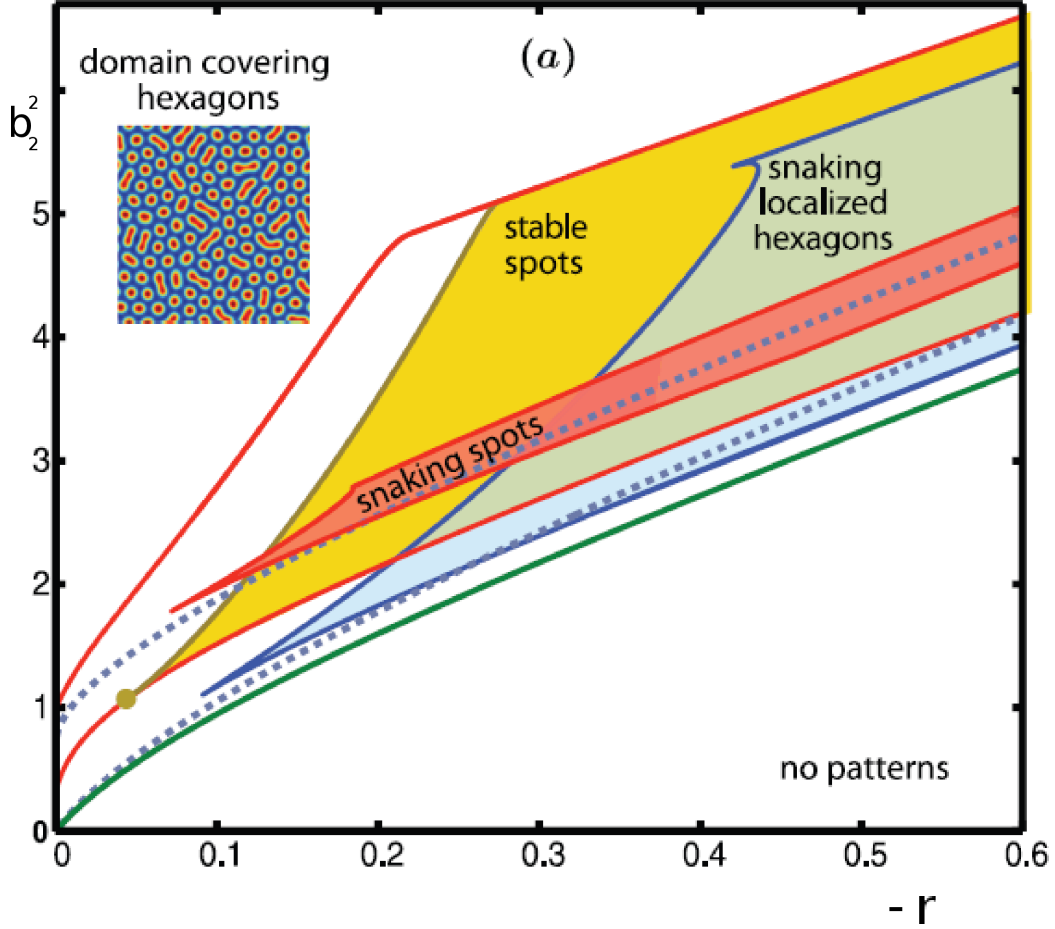
Figure 20: Localized hexagons, targets and spots in SH23. From [10].

phase slips [7]. We can describe the resulting phase-locked oscillations, including standard and reciprocal oscillons by examining the small amplitude

have been observed in the solutions of the FCGL equation for the amplitude of the phase-locked oscillation.

We suppose a dynamic observable $w(x,t)$ can be written in the form

$$w(x,t) = w_0 + A(\tilde{x}, \tilde{t})\mathrm{e}^{i\Omega t/2} + \text{c.c.} + ..., \qquad (28)$$

where w_0 is a steady homogeneous state of the system, $A(\tilde{x}, \tilde{t})$ is the (small) complex amplitude of the forced subharmonic response, and $\tilde{x}$ and $\tilde{t}$ are suitable slow spatial and temporal scales. The oscillation amplitude $A(\tilde{x}, \tilde{t})$ obeys the following evolution equation

$$A_{\tilde{t}} = (\mu + i\nu)A - (1 + i\beta)|A|^2 A + (1 + i\alpha)A_{\tilde{x}\tilde{x}} + \gamma\overline{A}, \qquad (29)$$

where μ represents the (small) distance from onset of a (supercritical) homogeneous oscillatory instability and γ is the (small) amplitude of the forcing. The coefficients α, β
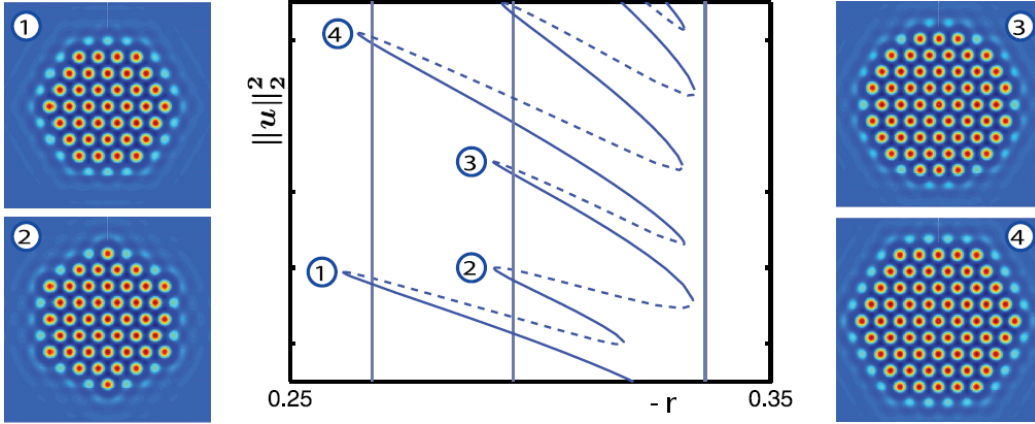
Figure 21: Bifurcation diagram for localized hexagons in SH23 showing the L_2 norm as a function of the bifurcation parameter $-r$. The sidepanels illustrate the solution profiles at the points labeled in the middle panel. Solid (dashed) lines indicate stable (unstable) solutions. From [10].

represent dispersion and nonlinear frequency correction, and are assumed to be $\mathcal{O}(1)$.[3] In the following we drop the tildes on $\tilde{x}$ and $\tilde{t}$.

Given the large number of parameters in equation (29), we expect that the system will display a wide range of behaviors. We restrict our attention to two cases corresponding to the parameter μ, namely when $\mu < 0$ and $\mu > 0$, respectively. In the case $\mu > 0$ the unforced system is self-exciting, but the free oscillations are damped when $\mu < 0$. In both cases, we assume that $\beta > 0$ and allow α to be positive or negative. The key observation is that the subharmonic forcing in the damped case creates a region of bistability between $A = 0$ and and a large amplitude phase-locked state A_u^+ with uniform amplitude [7]. Inside this region one expects localized states created by the same mechanism as in the Swift-Hohenberg equation.

We consider the damped case $\mu < 0$ in the (ν, γ) plane and find that a saddle-node bifurcation involving the uniform phase-locked states A_u^+ and A_u^- occurs at $\gamma = \gamma_b \equiv |\nu - \beta\mu|/\rho_\beta$, $\rho_\beta \equiv \sqrt{1 + \beta^2}$, whenever $\nu > \nu_\beta \equiv -\mu/\beta$. At this point, the uniform state has two zero spatial eigenvalues and two real nonzero spatial eigenvalues. Along the larger amplitude A_u^+ branch the zero eigenvalues split along the real axis and A_u^+ has two-dimensional stable and unstable manifolds. Thus localized states may exist in the form of orbits homoclinic to A_u^+. We calculate these as follows.

To find these states, we expand γ about the fold γ_b: $\gamma = \gamma_b + \epsilon^2 \delta$, where $\epsilon^2 \delta$ depends on the distance to the fold, $\epsilon \ll 1$ and $\delta > 0$. We solve the time-independent problem as in [7] (their Appendix C)

$$(\mathcal{L} + \mathcal{N}) \begin{bmatrix} U \\ V \end{bmatrix} = 0, \tag{30}$$

where $A = U + iV$, $\mathcal{L}$ is a linear operator and $\mathcal{N}$ is a nonlinear operator. Localized states

---

[3]Specifically if $\mu = \mathcal{O}(\epsilon^2)$ the forcing amplitude and frequency must satisfy $\gamma = \mathcal{O}(\epsilon^2)$, $\nu = \mathcal{O}(\epsilon^2)$ and the response satisfies $A = \mathcal{O}(\epsilon)$, $\tilde{x} = \epsilon x$ and $\tilde{t} = \epsilon^2 t$.

20

biasymptotic to A_u^+ take the form

$$\begin{bmatrix} U \\ V \end{bmatrix} = \begin{bmatrix} U \\ V \end{bmatrix}^+ + \begin{bmatrix} u \\ v \end{bmatrix}, \tag{31}$$

where the first term is the phase-locked state A_u^+ and the second term corresponds to space-dependent terms that decay to zero in the limit $x \to \pm\infty$. We can approximate A_u^+ by the series

$$\begin{bmatrix} U \\ V \end{bmatrix}^+ = \begin{bmatrix} U_0 \\ V_0 \end{bmatrix} + \epsilon \begin{bmatrix} U_1 \\ V_1 \end{bmatrix} + \epsilon^2 \begin{bmatrix} U_2 \\ V_2 \end{bmatrix} + ..., \tag{32}$$

where

$$\begin{bmatrix} U_0 \\ V_0 \end{bmatrix} = \begin{bmatrix} \eta_b \\ 1 \end{bmatrix} \Upsilon_0, \qquad \begin{bmatrix} U_1 \\ V_1 \end{bmatrix} = \sqrt{\delta} \begin{bmatrix} \xi_b \\ 1 \end{bmatrix} \Upsilon_1. \tag{33}$$

Here

$$\eta_b = \beta + \rho_\beta, \qquad \xi_b = \frac{\eta_b \nu + (1 - \beta\eta_b)|A_u(\gamma_b)|^2}{\nu - (\beta + \eta_b)|A_u(\gamma_b)|^2}, \tag{34}$$

$$\Upsilon_0 = \frac{|A_u(\gamma_b)|}{\sqrt{1 + \eta_b^2}}, \qquad \Upsilon_1 = \text{sgn}[\xi_b\eta_b + 1]\sqrt{\frac{\eta_b}{(\xi_b\eta_b + 1)(\xi_b - \eta_b)}}. \tag{35}$$

We expand the space-dependent second term in equation (31) as

$$\begin{bmatrix} u \\ v \end{bmatrix} = \epsilon \begin{bmatrix} u_1 \\ v_1 \end{bmatrix} + \epsilon^2 \begin{bmatrix} u_2 \\ v_2 \end{bmatrix} + ...,$$

noting that all the quantities in this equation depend on x in the slow spatial scale $X \equiv \epsilon^{1/2}x$. The linear operator in equation (30) can be written $\mathcal{L} = \mathcal{L}_0 + \epsilon\mathcal{L}_1 + \epsilon^2\mathcal{L}_2$, where

$$\mathcal{L}_0 = \begin{bmatrix} \mu + \gamma_b & -\nu \\ \nu & \mu - \gamma_b \end{bmatrix}, \qquad \mathcal{L}_1 = \begin{bmatrix} 1 & -\alpha \\ \alpha & 1 \end{bmatrix} \partial_{XX}, \qquad \mathcal{L}_2 = \begin{bmatrix} \delta & 0 \\ 0 & -\delta \end{bmatrix}. \tag{36}$$

The nonlinear terms can be written $\mathcal{N} = \mathcal{N}_0 + \epsilon\mathcal{N}_1 + \epsilon^2\mathcal{N}_2 + ...$, where

$$\mathcal{N}_0 = -\begin{bmatrix} U_0 & V_0 \end{bmatrix} \begin{bmatrix} U_0 \\ V_0 \end{bmatrix} \begin{bmatrix} 1 & -\beta \\ \beta & 1 \end{bmatrix}, \qquad \mathcal{N}_2 = -2\begin{bmatrix} U_0 & V_0 \end{bmatrix} \begin{bmatrix} U_1 + u_1 \\ V_1 + v_1 \end{bmatrix} \begin{bmatrix} 1 & -\beta \\ \beta & 1 \end{bmatrix}, \tag{37}$$

$$\mathcal{N}_2 = -\left\{ \begin{bmatrix} U_1 + u_1 & V_1 + v_1 \end{bmatrix} \begin{bmatrix} U_1 + u_1 \\ V_1 + v_1 \end{bmatrix} + 2\begin{bmatrix} U_0 & V_0 \end{bmatrix} \begin{bmatrix} U_2 + u_2 \\ V_2 + v_2 \end{bmatrix} \right\} \begin{bmatrix} 1 & -\beta \\ \beta & 1 \end{bmatrix}. \tag{38}$$

At order ϵ^0, the stationary solutions to equation (30) satisfy

$$\{\mathcal{L}_0 + \mathcal{N}_0\} \begin{bmatrix} U_0 \\ V_0 \end{bmatrix} = \begin{bmatrix} 0 \\ 0 \end{bmatrix}. \tag{39}$$

This equality can be determined from the definition of U_0 and V_0. At order ϵ, we have the following expression

$$\{\mathcal{L}_0 + \mathcal{N}_0\} \begin{bmatrix} U_1 + u_1 \\ V_1 + v_1 \end{bmatrix} = -\{\mathcal{L}_1 + \mathcal{N}_1\} \begin{bmatrix} U_0 \\ V_0 \end{bmatrix}. \tag{40}$$

21

The X-independent terms in this equation cancel (from the definition of U_1 and V_1), and we obtain

$$\left\{ \mathcal{L}_0 + \mathcal{N}_0 - 2 \begin{bmatrix} 1 & -\beta \\ \beta & 1 \end{bmatrix} \begin{bmatrix} U_0^2 & U_0 V_0 \\ U_0 V_0 & V_0^2 \end{bmatrix} \right\} \begin{bmatrix} u_1 \\ v_1 \end{bmatrix} = \begin{bmatrix} 0 \\ 0 \end{bmatrix}. \tag{41}$$

Hence, we write

$$\begin{bmatrix} u_1 \\ v_1 \end{bmatrix} = \begin{bmatrix} \xi_b \\ 1 \end{bmatrix} B(X), \tag{42}$$

where $B(X)$ is an unknown function of X. We proceed to order ϵ^2, obtaining

$$\{ \mathcal{L}_0 + \mathcal{N}_0 \} \begin{bmatrix} U_2 + u_2 \\ V_2 + v_2 \end{bmatrix} = -\{ \mathcal{L}_1 + \mathcal{N}_1 \} \begin{bmatrix} U_1 + u_1 \\ V_1 + v_1 \end{bmatrix} - \{ \mathcal{L}_2 + \mathcal{N}_2 \} \begin{bmatrix} U_0 \\ V_0 \end{bmatrix}. \tag{43}$$

As previously, the X-independent terms cancel. To obtain the solvability condition for this equation, we take the scalar product with

$$\Xi_b = \begin{bmatrix} -\eta_b & 1 \end{bmatrix}, \tag{44}$$

and eliminate the u_2, v_2 terms, so that

$$a_b B_{XX} = b_b (2 V_1 B + B^2). \tag{45}$$

Here,

$$a_b = 1 + \alpha \xi_b + \alpha \eta_b - \eta_b \xi_b, \qquad b_b = -\frac{\Upsilon_0 (1 + \eta_b^2)}{\Upsilon_1^2}, \tag{46}$$

and we must have $b_b < 0$. Equation (45) yields either spatially homogeneous solutions $B = -2V_1$, or the solution

$$\begin{bmatrix} U \\ V \end{bmatrix} = \begin{bmatrix} U_0 \\ V_0 \end{bmatrix} - \epsilon \begin{bmatrix} U_1 \\ V_1 \end{bmatrix} + ..., \tag{47}$$

corresponding to the other branch of uniform phase-locked states, A_u^-. Equation (45) also possesses X-dependent solutions of the form

$$B(X) = -3 \Upsilon_1 \sqrt{\delta} \operatorname{sech}^2 \left\{ \left(\frac{\Upsilon_1 \sqrt{\delta}}{2 a_b / b_b} \right)^{1/2} X \right\}. \tag{48}$$

These correspond to the solution

$$\begin{bmatrix} U \\ V \end{bmatrix} = \begin{bmatrix} U \\ V \end{bmatrix}^+ - 3 \Upsilon_1 \sqrt{\gamma - \gamma_b} \begin{bmatrix} \xi_b \\ 1 \end{bmatrix} \operatorname{sech}^2 \left\{ (\gamma - \gamma_b)^{1/4} \left(\frac{\Upsilon_1}{2 a_b / b_b} \right)^{1/2} x \right\}, \tag{49}$$

describing reciprocal oscillons, i.e., 'holes' in an otherwise uniformly oscillating state. If this state is followed numerically one finds that the holes deepen and fill with the trivial state $A = 0$. Pinning is absent since the spatial eigenvalues of A_u^+ are real.

Other localized states are also present and these are discussed in [7].

References

[1] D. Avitabile, D. J. B. Lloyd, J. Burke, E. Knobloch and B. Sandstede. To snake or not to snake in the planar Swift-Hohenberg equation. *SIAM J. Appl. Dyn. Sys.*, **9**, pp. 704–733, 2010.

[2] M. Beck, J. Knobloch, D. J. B. Lloyd, B. Sandstede and T. Wagenknecht. Snakes, ladders and isolas of localized patterns. *SIAM J. Math. Anal.* **41**, pp. 936–972, 2009.

[3] J. R. Burke. Localized States in Driven Dissipative Systems. PhD Thesis, University of California at Berkeley, 2008.

[4] J. Burke, S. M. Houghton and E. Knobloch. Swift-Hohenberg equation with broken reflection symmetry. *Phys. Rev. E* **80**, 036202, 2009.

[5] J. Burke and E. Knobloch. Homoclinic snaking: structure and stability. *Chaos* **17**, 037102, 2007.

[6] J. Burke and E. Knobloch. Localized states in the generalized Swift–Hohenberg equation. *Phys. Rev. E* **73**, 056211, 2006.

[7] J. Burke, A. Yochelis and E. Knobloch. Classification of spatially localized oscillations in periodically forced dissipative systems. *SIAM J. Appl. Dyn. Sys.* **7**, pp. 651–711, 2008.

[8] R. B. Hoyle. *Pattern Formation: An Introduction to Methods*, Cambridge University Press, 2006.

[9] G. Kozyreff and S. J. Chapman. Asymptotics of large bound states of localized structures. *Phys. Rev. Lett.* **97**, 044502, 2006.

[10] D. J. B. Lloyd, B. Sandstede, D. Avitabile and A. R. Champneys. Localized hexagon patterns of the planar Swift-Hohenberg equation. *SIAM J. Appl. Dyn. Sys.* **7**, pp. 1049–1100, 2008.

[11] D. J. B. Lloyd and B. Sandstede. Localized radial solutions of the Swift-Hohenberg equation. *Nonlinearity*, **22**, pp. 485–524, 2009.

[12] S. McCalla and B. Sandstede. Snaking of radial solutions of the multi-dimensional Swift-Hohenberg equation: A numerical study. *Physica D* **239**, pp. 1581–1592, 2010.

[13] Y. Pomeau. Front motion, metastability and subcritical bifurcations in hydrodynamics. *Physica D* **23**, pp. 3–11, 1986.

[14] W. van Saarloos. Front propagation into unstable states. *Phys. Rep.* **386**, pp. 29–222, 2003.

[15] P. D. Woods and A. R. Champneys. Heteroclinic tangles and homoclinic snaking in the unfolding of a degenerate reversible Hamiltonian-Hopf bifurcation. *Physica D* **129**, pp. 147–170, 1999.